

Transitions of bouncing and coalescence in binary droplet collisions

Kuan-Ling Huang¹ and Kuo-Long Pan^{1,†}

¹Department of Mechanical Engineering, National Taiwan University, Taipei 10617, Taiwan, ROC

(Received 25 September 2020; revised 4 August 2021; accepted 8 September 2021)

In droplet impacts, transitions between coalescence and bouncing are determined by complex interplays of multiple mechanisms dominating at various length scales. Here we investigate the mechanisms and governing parameters comprehensively by experiments and scaling analyses, providing a unified framework for understanding and predicting the outcomes when using different fluids. Specifically, while bouncing had not been observed in head-on collisions of water drops under atmospheric conditions, it was found in our experiments to appear on increasing the droplet diameter sufficiently. Contrarily, while bouncing was always observed in head-on impacts of alkane drops, we found it to disappear on decreasing the diameter sufficiently. The variations are related to gas draining dynamics in the inter-droplet film and suggest an easier means for controlling bouncing as compared to alternating the ambient pressure usually sought. The scaling analysis further shows that for a given Weber number, enlarging droplet diameter or fluid viscosities, or lowering surface tension contributes to a larger characteristic minimum thickness of the gas film, thus enhancing bouncing. The key dimensionless group ($Oh_{g,l}$, Oh_l , A^*) is identified, referred to as the two-phase Ohnesorge number, the Ohnesorge number of liquid and the Hamaker constant, respectively. Our thickness-based model indicates that as $h'_{m,c} > 21.1h_{cr}$, where $h'_{m,c}$ is the maximum value of the characteristic minimum film thickness ($h_{m,c}$) and h_{cr} is the critical thickness, bouncing occurs in both head-on and off-centre collisions. That is, when $1.2Oh_{g,l}/(1 - 2Oh_l) > \sqrt[3]{A^*}$, a fully developed bouncing regime occurs, thereby yielding a lower coalescence efficiency. The transitional Weber number is found universally to be 4.

Key words: breakup/coalescence, drops

† Email address for correspondence: panpeter@ntu.edu.tw

© The Author(s), 2021. Published by Cambridge University Press. This is an Open Access article, distributed under the terms of the Creative Commons Attribution licence (<https://creativecommons.org/licenses/by/4.0/>), which permits unrestricted re-use, distribution, and reproduction in any medium, provided the original work is properly cited.

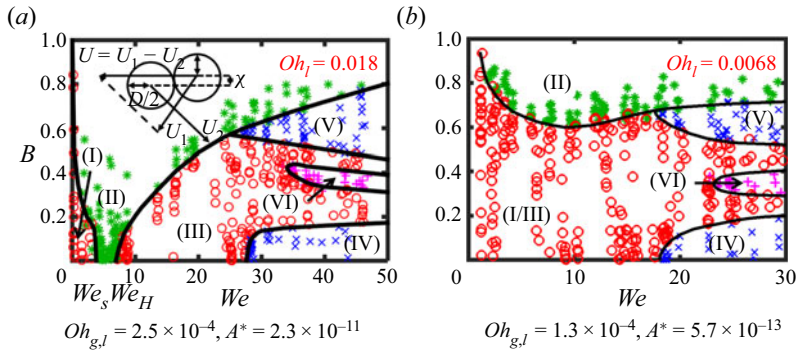


Figure 1. The regime diagrams in terms of the present experimental results of (a) dodecane and (b) water drops with a diameter 300 μm , showing a fully developed and partially developed bouncing regime, respectively. The symbols for indicating the regimes are: red circle, coalescence; blue cross, stretching/reflexive separation; green asterisk, bouncing; pink plus, rotational separation.

1. Introduction

Droplet collisions have been extensively studied in past decades (Ashgriz & Poo 1990; Jiang, Umemura & Law 1992; Qian & Law 1997; Estrade *et al.* 1999; Brenn, Valkovska, & Danov 2001; Pan, Law & Zhou 2008; Pan, Chou & Tseng 2009; Zhang & Law 2011; Tang, Zhang, & Law 2012; Kwakkel, Breugem, & Boersma 2013; Huang & Pan 2015; Li 2016; Pan *et al.* 2016, 2019; Sommerfeld & Kuschel 2016; Hu *et al.* 2017; Al-Dirawi & Bayly 2019; Huang, Pan & Josserand 2019; Chubynsky *et al.* 2020) due to significant relevance to a variety of systems in natural and technological situations. Examples are seen in raindrop formation (Gunn 1965; Strangeways 2006), medical therapy (May 1973; Feng *et al.* 2016), disease transmission (Tellier 2009; Gralton *et al.* 2011) and combustion processes in engines (Chiu 2000; Zhang *et al.* 2016). Typically, the collision outcomes of two identical droplets can be mapped in the regime diagrams depicted by a Weber number ($We = \rho_l U^2 D / \sigma$) and an impact parameter ($B = \chi / D = \sin \theta$). They show coalescence after minor deformation (I), bouncing (II), coalescence after substantial deformation (III), reflexive separation (IV), stretching separation (V) (Ashgriz & Poo 1990; Qian & Law 1997) and rotational separation (VI) (Pan *et al.* 2019). Here We indicates the ratio of impact inertia and surface tension force and B represents the effect of the colliding angle (θ) between the droplets. The inset of figure 1(a) shows a schematic for definitions of the collision parameters, where D denotes the droplet diameter, ρ_l and σ the density and surface tension of liquid, respectively, and χ the projection of the separation distance between the droplet centres in the direction normal to the relative velocity U .

A typical regime diagram of alkane drops is shown in figure 1(a), featuring a fully developed bouncing regime (FB) where bouncing extends to $B=0$. That is, non-monotonic transitions of regime (I)–(II)–(III) can be found by increasing We from $O(0.1)$ to $O(10)$ in both head-on and off-centre collisions. Here We_S and We_H denote the transition boundaries from regime (I) to (II) and from (II) to (III) at $B=0$, respectively, for soft and hard collisions (Pan *et al.* 2008). Compared with alkane drops, bouncing is not observed for head-on collisions (named partially developed bouncing regime, PB) of drops with high surface tension, such as water, as shown in figure 1(b). Such a distinction in the patterns of water and hydrocarbons was not realized until the discovery of the effect of the ambient gas pressure (Qian & Law 1997). Specifically, it was reported that increasing the gas density by raising the pressure or molecular weight of the ambient gas promotes

bouncing and widens regime (II), while the opposite holds when reducing the density. As such, compared to atmospheric conditions, the bouncing regime is eliminated for alkane droplets on steadily decreasing the ambient pressure to 0.6 atm and it emerges for water droplets as the pressure is increased to 2.7 atm (Qian & Law 1997). Consequently, the key role of the inter-droplet gaseous film is revealed, whose development determines whether the impinging drops will rebound or merge. However, the influences of liquid properties on bouncing and coalescence regimes are not explicitly elucidated.

In addition to the surrounding gas properties, variation of the gas dynamics in the intervening gap and subsequently the propensity for bouncing are also found by adding surfactant into aqueous drops (Pan *et al.* 2016) and changing the liquid viscosity (μ_l) (Sommerfeld & Kuschel 2016; Hu *et al.* 2017; Al-Dirawi & Bayly 2019). Moreover, increasing the droplet diameter was found preliminarily in our prior experiment (Huang & Pan 2015) and a numerical simulation (Li 2016) to enlarge the range between We_S and We_H for alkane drops. Li (2016) indicated that the drop size effect on the bouncing phenomenon can be attributed to the competition between the capillary number ($Ca_g = \mu_g U / \sigma = \mu_g We / \sqrt{\rho_l D \sigma}$) and dimensionless mean free path ($\bar{\lambda} = \lambda / D$), while the influence of $\bar{\lambda}$ consequentially determines the occurrence of droplet bouncing. Here μ_g is the gas viscosity and λ is the mean free path of gas. Compared with the other transitions involving merely hydrodynamically dominating phenomena such as coalescence to various types of separations which can be described based on the conservation laws (Ashgriz & Poo 1990; Jiang *et al.* 1992; Qian & Law 1997) using macroscopic fluid parameters, theoretical models for prediction of bouncing are relatively scarce. This is mainly due to the sophisticated interplays of multiple factors dominating the collision process which spans a wide range of length scales, involving distinct mechanisms specifically regarding the continuum and rarefied gas dynamics as well as compressibility and intermolecular forces (Pan *et al.* 2008). As a consequence, the underlying parameters and their effects on bouncing cannot be comprehended in an explicit way by phenomenological models that provide correlations of the key dimensionless groups.

While some insights were gained in a few theoretical analyses tackling the whole set of governing equations or models (Gopinath, Chen & Koch 1997; Gopinath & Koch 2002), the parametric influence on the regime diagrams is not available until substantial computations are conducted, even merely for head-on collisions. There are few phenomenological models developed to predict the transitions between bouncing and coalescence, based on the criterion of energy balance, stating that bouncing occurs if the initial kinetic energy does not exceed the surface energy required to produce the maximum deformation (Estrade *et al.* 1999; Hu *et al.* 2017; Al-Dirawi & Bayly 2019). They predict We_H without describing We_S and the non-monotonic transitions of regimes (I)–(II)–(III), by which the effects of liquid viscosity (Hu *et al.* 2017; Al-Dirawi & Bayly 2019) and surface deformation (Estrade *et al.* 1999; Hu *et al.* 2017; Al-Dirawi & Bayly 2019) are considered. Notwithstanding, the roles of μ_g and van der Waals (vdW) attraction are ignored, which are believed to play critical roles in causing repulsive pressure in the gas film and dominating droplet merging, respectively (Pan *et al.* 2008; Zhang & Law 2011; Kwakkel *et al.* 2013; Li 2016; Chubynsky *et al.* 2020), and hence should be accounted for in the bouncing process.

These results reveal significant difficulty for predicting the transitions of bouncing and coalescence due to the inherent complexity underlying the non-monotonic transitions from regimes (I) to (III) and that We alone would not be the sole parameter to describe the criteria. In the present study, we provide the first experimental evidence that the droplet size alone can change the bouncing regime essentially and hence the pattern

Authors	We	D (μm)	Oh_l (10^{-3})	$Oh_{g,l}$ (10^{-4})	A^* (10^{-13})
Jiang <i>et al.</i> (1992)	0–100	300	6–44	2.4–2.8	22–27
Tang <i>et al.</i> (2012)	0–70	200	9–36	2.2–2.8	128–491
Sommerfeld & Kuschel (2016)	10–180	370	15–282	1.9–2.3	129–146
Finotello <i>et al.</i> (2018)	10–200	700	22–438	0.8–1.0	—
Huang & Pan (2015)	0–50	300, 600	8–39	1.7–2.6	55–218
Al-dirawi & Bayly (2019)	0–90	375	21–221	1.4–1.5	—
Present study	0–40	160, 230, 300, 600, 700, 1000	3–51	0.7–3.6	5.1–821

Table 1. The ranges of the dimensionless parameters used in the present and previous studies.

of the We – B diagram. Specifically, by increasing D sufficiently, bouncing is observed in head-on collisions of water drops and, conversely, by decreasing D this regime is eventually annihilated in the head-on impacts of hydrocarbon drops. Consequently, in a way similar to that of the variation of ambient pressure (Qian & Law 1997; Reitter *et al.* 2017), the forms of regime diagrams are unified for different liquids. Table 1 summarizes the ranges of the present key parameters that were covered in previous experimental studies, where $A^* = A_H/\sigma D^2$, $Oh_l = \mu_l/\sqrt{\rho_l D \sigma}$ and $Oh_{g,l} = \mu_g/\sqrt{\rho_l D \sigma}$ are the dimensionless Hamaker constant, Ohnesorge number of liquid and two-phase Ohnesorge number, respectively. Here $Oh_{g,l}$ was shown by Li (2016) to describe the droplet deformation. Table 1 shows that the range of A^* in our study spans two orders of magnitude (5.1×10^{-13} – 8.2×10^{-11}), which is the largest range among the parameters. Furthermore, the range of the present $Oh_{g,l}$ data is also the widest (7.0×10^{-5} – 3.6×10^{-4}) compared with other studies.

These scenarios can be comprehended by our scaling analyses for estimating the characteristic minimum gas-film thickness ($h_{m,c}$), which has not been derived in previous studies of droplet bouncing after impact (Jiang *et al.* 1992; Qian & Law 1997; Klaseboer, Manica & Chan 2014; de Ruyter *et al.* 2015). By considering viscous dissipation in the drops and using a different scaling of $\partial h/\partial t$ in the lubrication equation, we have derived the key dimensionless parameters and give a criterion for prediction of bouncing for a wide range of fluid properties.

2. Experimental set-up

To set up the experiment, identical droplets of decane, dodecane, tetradecane or water were generated separately from two glass nozzles with fixed diameters by the conventional drop-on-demand method (Pan *et al.* 2009, 2016, 2019; Huang & Pan 2015; Huang *et al.* 2019). The properties of the tested liquids are listed in table 2, including a large range of surface tensions (23.8–72.0 mN m⁻¹) and droplet diameters (160–1000 μm). In addition, the Hamaker constants of the liquids used in the present study are estimated by the Lifshitz theory (Lifshitz 1956; Israelachvili 2011). The relative velocity of colliding droplets can be controlled by the amplitude of periodic electric pulses and D can be finely adjusted ($\pm 1.6\%$) by the electrical pulse width. We note that droplets with $D = 1000 \mu\text{m}$ cannot be made due to the effect of gravity if the droplets are squeezed out horizontally from the nozzles, as demonstrated in previous experimental works (Ashgriz & Poo 1990; Jiang *et al.* 1992; Qian & Law 1997; Pan *et al.* 2008, 2009, 2016, 2019; Tang *et al.* 2012; Huang & Pan 2015; Sommerfeld & Kuschel 2016; Huang *et al.* 2019). To overcome this

Bouncing/coalescence transitions in binary droplet collisions

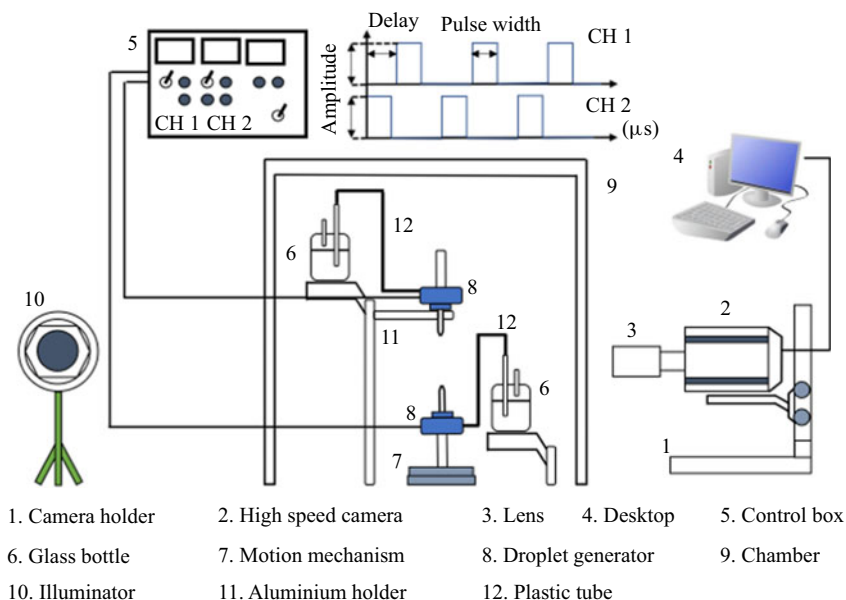


Figure 2. Experiment set-up for collisions of droplets with a diameter 1000 μm .

	Decane	Dodecane	Tetradecane	Water	Glycerol (60 wt%)
Density (kg m^{-3})	728	750	759	998	1152
Viscosity (mPa s)	0.82	1.33	2.05	0.92	10.9
Surface tension (mN m^{-1})	23.8	24.9	26.0	72.0	66.0
Diameter (μm)	160/300/600	160/300/600	160/230/300/600	300/700/1000	450
Hamaker constant (J)	5.0×10^{-20}	5.0×10^{-20}	5.2×10^{-20}	3.7×10^{-20}	—

Table 2. Properties of tested liquids (25 °C).

restriction, we adopted another experimental set-up, as shown in figure 2, by squeezing out droplets vertically (Pan *et al.* 2009) such that droplets with $D = 1000 \mu\text{m}$ can be made and the collisions were accomplished in the vertical plane. Via appropriate settings for the separation distance between the two nozzles and the delay time between two electrical pulses, droplets with a diameter of 1000 μm can be made sufficiently spherical and stable before each collision event. It is noted that since the Bond number ($Bo = \rho_l g D^2 / \sigma$, where g is the gravitational acceleration) of a 1.0 mm droplet is as small as 0.136 for water, the influence of gravity on droplet deformation can be neglected. The experimental images in figure 3 demonstrate ostensible sphericity for the droplets before impact.

Time-resolved images were recorded by a high-speed CMOS digital camera (Vision Research, Phantom M310), which supported a resolution of 512×512 pixels up to 10 000 frames per second. A microscope lens (Navitar 6.5X) was mounted on the camera for increasing the spatial resolution up to 200 pixels mm^{-1} . The exposure time of the shutter can be set down to 1 μs to avoid blurring due to background scattering. Surface tension of the tested liquids was measured by a tensiometer (DCAT, DataPhysics Instruments GmbH)

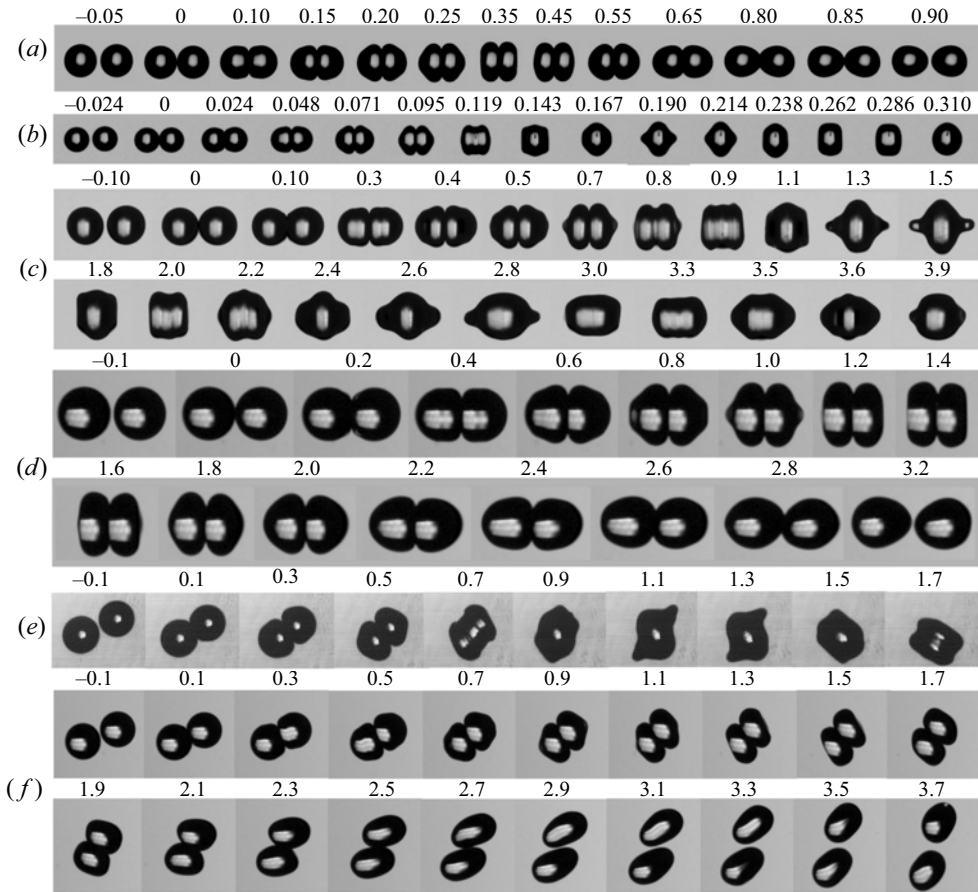


Figure 3. Collision sequences of dodecane drops with (a) $D = 300 \mu\text{m}$ at $We = 4.60$, $B = 0$, (b) $D = 160 \mu\text{m}$ at $We = 4.70$, $B = 0$, and of water drops with (c) $D = 700 \mu\text{m}$ at $We = 4.73$, $B = 0$, (d) $D = 1000 \mu\text{m}$ at $We = 4.74$, $B = 0$, (e) $D = 700 \mu\text{m}$ at $We = 4.68$, $B = 0.33$ and (f) $D = 1000 \mu\text{m}$ at $We = 4.77$, $B = 0.32$. Time unit: milliseconds.

with an accuracy of $\pm 0.05 \text{ mN m}^{-1}$ and the viscosity by a rheometer (Brookfield DV3 T, AMETEK Inc.) with an accuracy of $\pm 0.01 \text{ mPa s}$. The uncertainties of We and B are $\pm 3.7\%$ and $\pm 1.6\%$, respectively. In addition, the viscosity of air (μ_g) is taken to be 0.0186 mPa s . Our experiments were carried out at room temperature (25°C) and at a relative humidity of 48% . More experimental details are provided in [Appendix A](#).

3. Results and discussion

3.1. Experimental results

[Figure 3\(a\)](#) shows the collision sequence of dodecane drops with diameters of $300 \mu\text{m}$ at $We = 4.6$, indicating that the colliding drops bounce away at $t = 0.9 \text{ ms}$. Given almost the same We , however, the collision sequence with a smaller drop size ($D = 160 \mu\text{m}$) exhibits an entirely different outcome from that expected in [figure 1\(a\)](#). That is, the drops merge at $t \sim 0.119 \text{ ms}$, as shown in [figure 3\(b\)](#). The same scenario resulting from the variation of droplet size is also found for water. Specifically, in contrast to coalescence of two water

Bouncing/coallescence transitions in binary droplet collisions

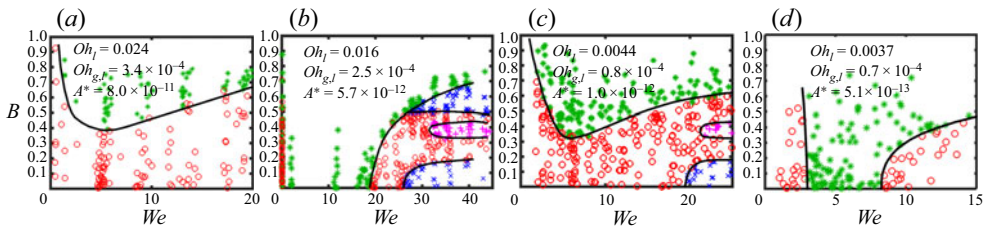


Figure 4. Regime diagrams for dodecane drops with diameters of (a) 160 and (b) 600 μm , and for water drops with diameters of (c) 700 and (d) 1000 μm .

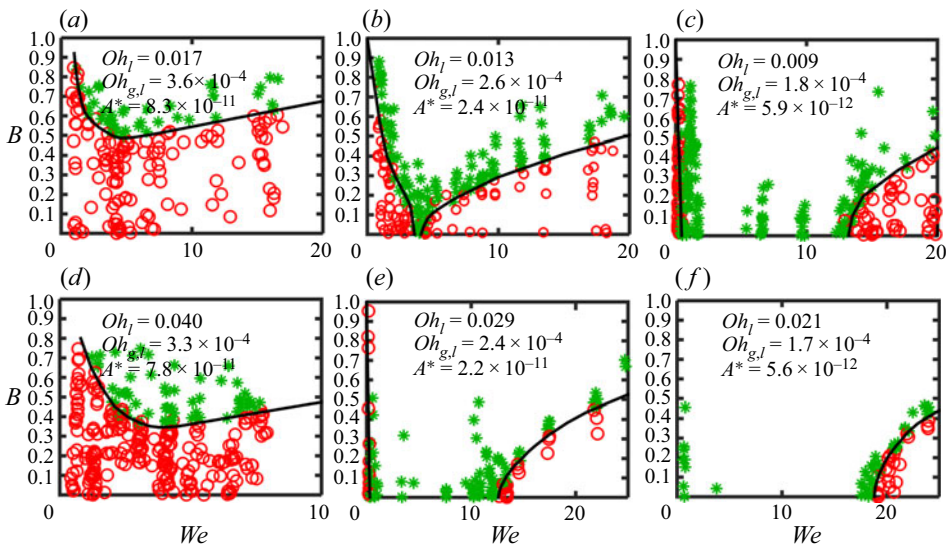


Figure 5. Regime diagrams for decane drops with (a) $D = 160 \mu\text{m}$, (b) $300 \mu\text{m}$ and (c) $600 \mu\text{m}$; for tetradecane drops with (d) $D = 160 \mu\text{m}$, (e) $300 \mu\text{m}$ and (f) $600 \mu\text{m}$.

drops with $D = 700 \mu\text{m}$ at $We = 4.73$ (figure 3c), they bounce away when D is increased to $1000 \mu\text{m}$ (figure 3d). Moreover, the droplet size effect on the bouncing regime can also be found in off-centre collisions. Figure 3(e) shows that at $We = 4.68$, water drops with $D = 700 \mu\text{m}$ merge at $t \sim 0.7$ ms. However, at a similar value of We , when the diameter of the two water drops increases to $1000 \mu\text{m}$, bouncing occurs after impact (figure 3f). This regime has never been observed in the literature for head-on collisions of water droplets (Ashgriz & Poo 1990; Tang, Zhang & Law 2012; Huang & Pan 2015; Li 2016; Pan *et al.* 2019).

The regime diagrams with varying drop diameters of dodecane and water are shown in figure 4. Compared to the typical regime diagram of alkanes shown in figure 1(a), bouncing is absent in head-on collisions of dodecane drops with diameters of $160 \mu\text{m}$ (figure 4a). In contrast, when the droplet diameter is increased to $600 \mu\text{m}$, the bouncing regime is dramatically enlarged and covers a substantial range of We at $B = 0$ (figure 4b). For water drops, the bouncing tendency is also promoted by increasing droplet diameter. As compared with figure 1(b), figure 4(c) shows that regime (II) occurs beyond $B \sim 0.32$ for the case of $D = 700 \mu\text{m}$ while the minimum B is up to ~ 0.6 for $D = 300 \mu\text{m}$. Consequently, when the droplet diameter is further increased to $1000 \mu\text{m}$, as shown in

figure 4(d), a fully developed regime (II) can be observed, which is similar to the typical regime diagram of alkanes. The effect of varying D on regime (II) is also valid for other alkanes as shown in figure 5. With a droplet size as small as $D = 160 \mu\text{m}$ for decane (figure 5a) and tetradecane (figure 5d), bouncing is not observed in head-on collisions, similar to the outcome for water drops usually reported (Ashgriz & Poo 1990; Qian & Law 1997; Estrade *et al.* 1999; Pan *et al.* 2008). When the diameter is increased to $300 \mu\text{m}$, the bouncing regime becomes fully developed, as shown in figures 5(b) and 5(e). By further increasing D to $600 \mu\text{m}$ (figure 5c,f), regime (II) is significantly expanded in the range $We < 20$ with a much larger We_H than that of $D = 300 \mu\text{m}$. These results clearly demonstrate that bouncing can be suppressed by decreasing the droplet diameter but encouraged by increasing it. This fact shows an analogous effect to changing the pressure of ambient gas (Qian & Law 1997; Reitter *et al.* 2017), which could, however, be executed with much less effort, providing an appealing solution to manipulating bouncing readily.

3.2. Scaling analysis

3.2.1. Governing factors

To find the key dimensionless groups governing the development of bouncing in the regime diagrams, we consider the dynamics of the gas film formed between two approaching drops in head-on collisions. Previous studies have shown that coalescence occurs when the minimum thickness of the film (h_m) is so small that vdW attraction can dominate the progress of approach (Pan *et al.* 2008; Zhang & Law 2011; Kwakkel *et al.* 2013; Li 2016; Chubynsky *et al.* 2020). In this regard, via the stress balance at the rim of the gas film at the stage when the interface is slightly deformed (figure 6b), we first estimate the characteristic minimum thickness of the gas film ($h_{m,c}$) for each collision event. The scaling process is similar to that of a previous study that predicts the dimple height between an impinging drop and a solid surface (Klaseboer *et al.* 2014), whereas viscous dissipation is considered in the present impact of binary drops. The normal stress balance at the liquid–gas interface shows that

$$p_{g,r} + \frac{\sigma}{r} \frac{\partial}{\partial r} \left(r \frac{\partial h}{\partial r} \right) = p_{l,r}. \quad (3.1)$$

In (3.1), the pressure in the liquid at the rim, $p_{l,r}$, is obtained from the simplified momentum equation (the derivation of which can be seen in Appendix C) along a streamline from the top to the rim of the drop, as shown in figure 6(b). As a consequence, $p_{l,r}$ can be written as

$$p_{l,r} \simeq \frac{2\sigma}{R} + \frac{1}{2} \rho_l U'^2. \quad (3.2)$$

Here U' is the velocity at the top of the drop, which can be obtained from the energy conservation, showing that

$$SE_0 + \frac{1}{2} \left(\frac{4}{3} \pi R^3 \right) \rho_l U^2 = SE_1 + \frac{1}{2} \left(\frac{4}{3} \pi R^3 \right) \rho_l U'^2 + \mu_l \int_0^\tau \int_0^\tau \frac{1}{2} \left[\frac{\partial u_i}{\partial x_j} + \frac{\partial u_j}{\partial x_i} \right]^2 dt dx^3. \quad (3.3)$$

Here SE_0 is the surface energy before droplet impact and SE_1 is that at the stage with a small deformation. As justified by comparing the experimental images shown in figure 6, since the drop deformation is relatively small in the latter and the surface energy at the

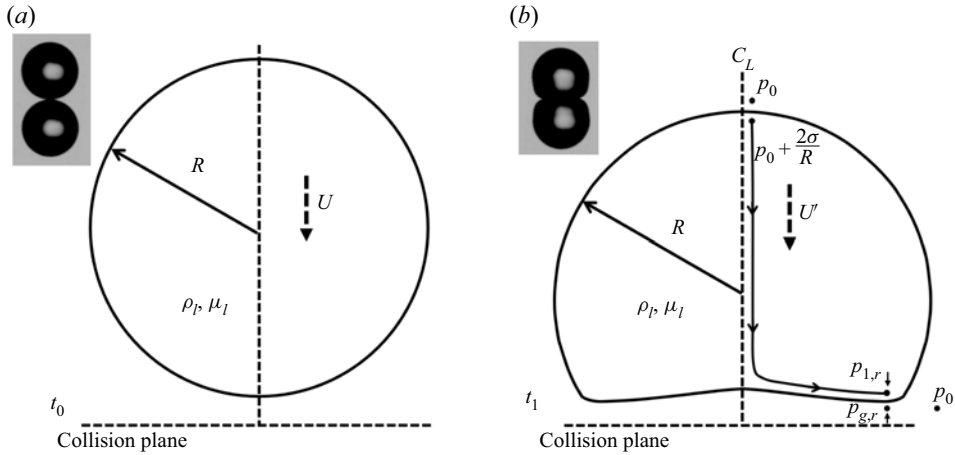


Figure 6. Schematic of a drop impacting a solid surface or another drop at the stage (a) before impact and (b) with a slight deformation.

largest deformation (figure 3) is only about 16 % larger than the initial surface energy (Pan *et al.* 2008), the difference between SE_0 and SE_1 can be neglected. By considering $\tau = R/U$ as the time scale, U the velocity scale and R the length scale, (3.3) becomes

$$\frac{1}{2}\rho_l U^2 = \frac{1}{2}\rho_l U^2 - \frac{2\mu_l U}{R}. \tag{3.4}$$

The pressure in the gas film at the rim, $p_{g,r}$, is estimated by the Stokes–Reynolds lubrication equation associated with the assumption of immobile liquid–gas interfaces, showing

$$\frac{\partial h}{\partial t} = \frac{1}{12\mu_g} \frac{1}{r} \frac{\partial}{\partial r} \left(rh^3 \frac{\partial p_{g,r}}{\partial r} \right). \tag{3.5}$$

The lubrication equation assumes that the characteristic length scale of the film thickness is significantly smaller than the film/drop radius, leading to negligibility of the inertial flow in the film. For the gas film between two approaching droplets, the film thickness is at least 100 times smaller than the droplet diameter (Pan *et al.* 2008), satisfying this assumption. Moreover, previous numerical simulations based on the lubrication equation have shown good agreement with experimental images and indicated that the influence of gas density on droplet bouncing can be neglected (Zhang & Law 2011; Li 2016; Chubynsky *et al.* 2020). Regarding the mobility of the liquid–gas interface, since the liquid viscosity is much higher than the air viscosity (Yiantsios & Davis 1990), and prior studies have experimentally suggested that the interfaces of drops or bubbles usually behave as tangentially immobile surfaces (Manica *et al.* 2010; Parkinson & Ralston 2010; Manica & Chan 2011), we have assumed immobile liquid–gas interfaces. With $t \sim R/U$, $h \sim h_{m,c}$ and $r \sim \sqrt{Rh_{m,c}}$, (3.5) becomes

$$\frac{h_{m,c} U}{R} \simeq \frac{h_{m,c}^2 p_{g,r}}{12R\mu_g}, \tag{3.6}$$

and $p_{g,r}$ can be shown as

$$p_{g,r} \simeq \frac{12\mu_g U}{h_{m,c}}. \tag{3.7}$$

By combining (3.1), (3.2), (3.4) and (3.7), the scaling relation is obtained as

$$\frac{12\mu_g U}{h_{m,c}} \simeq \frac{\sigma}{R} + \frac{1}{2}\rho_l U^2 - \frac{2\mu_l U}{R}. \quad (3.8)$$

Thus (3.8) becomes

$$h_{m,c} \simeq \frac{12\mu_g U}{\frac{\sigma}{R} + \frac{1}{2}\rho_l U^2 - \frac{2\mu_l U}{R}} = \frac{12\mu_g UD/\sigma}{2 + \frac{1}{2}\rho_l U^2 D/\sigma - 4\mu_l U/\sigma} = \frac{24Oh_{g,l}D\sqrt{We}}{4 + We - 8Oh_l\sqrt{We}} \quad (3.9)$$

and

$$H_{m,c}(We) \simeq \frac{24Oh_{g,l}\sqrt{We}}{We + 4 - 8Oh_l\sqrt{We}}, \quad (3.10)$$

where $H_{m,c}$ is the dimensionless form of $h_{m,c}$. Here $Oh_{g,l} = \mu_g/\sqrt{\rho_l D\sigma} = Ca_g We^{-0.5}$, which is the newly derived two-phase Ohnesorge number.

In contrast to the present scaling analysis, Klaseboer *et al.* (2014) ignored the coefficient 1/12 in (3.5) and scaled the term $\partial h/\partial t$ as U , and the Laplace pressure as σ/R , leading to the result of $h_{m,c} \simeq (D/2)\sqrt{2Oh_{g,l}\sqrt{We}/(2 + We + 0.5Bo)}$. Here we have kept the coefficient 1/12 and scaled $\partial h/\partial t$ as $h_{m,c}/(R/U)$, and the Laplace pressure as $2\sigma/R$. This yields the results that our $h_{m,c}$ values are about 3 times smaller than the dimple height predicted by Klaseboer *et al.* (2014), which are closer to previous numerical results (Pan *et al.* 2008). Moreover, with the scaling of Laplace pressure $2\sigma/R$, the transitional We from PB to FB is derived.

3.2.2. Universal phenomena in drop impacts

Figure 7(a) plots $h_{m,c}$ as a function of We in (3.9) for different properties of drops, showing that $h_{m,c}$ initially increases and then decreases as We increases. The non-monotonic trend of $h_{m,c}$ - We curves is similar to the variations of dimple height and the minimum thickness scaled in Pan (2004), Pan & Law (2004) and Klaseboer *et al.* (2014). Strikingly, without any empirical factor, the $h_{m,c}$ values exhibit the same order of magnitude as a previous numerical prediction based on the continuum assumption (Pan *et al.* 2008) but they are one order of magnitude larger than those of the simulations including rarefied gas effect (Zhang & Law 2011; Kwakkel *et al.* 2013; Li 2016; Chubynsky *et al.* 2020). Furthermore, by taking the derivative $dh_{m,c}/dWe = 0$, we can find the maximum $h_{m,c}(We)$, $h'_{m,c} = 6Oh_{g,l}D/(1 - 2Oh_l)$, at $We = 4$, which is denoted by We' , for every set of drops with any given $Oh_{g,l}$ and Oh_l . To further identify the transitional We from PB to FB experimentally, we have obtained the regime diagrams of tetradecane drops with $D = 230 \mu\text{m}$ and drops of a glycerol solution with $D = 450 \mu\text{m}$, as shown in the figure 8. It is observed that a small range of bouncing intervenes in head-on collisions ($We = 2.0\text{--}4.5$). Therefore, we can estimate the transitional We by the average of We_S and We_H , i.e. $We' = 3.3$. This is quite close to the universal value as derived.

Equation (3.9) shows that when $We \ll We'$ ($\frac{1}{2}\rho_l U^2 \ll \sigma/R$ and $2\mu_l U/R \ll \sigma/R$), $h_{m,c}$ is dominated by the ratio between $12\mu_g U$ and σ/R , and thus increases with We ($h_{m,c} \propto Oh_{g,l}D\sqrt{We}$). On the other hand, when $We \gg We'$ ($\frac{1}{2}\rho_l U^2 \gg \sigma/R$ and $\frac{1}{2}\rho_l U^2 \gg 2\mu_l U/R$), $h_{m,c}$ is dominated by the ratio between $12\mu_g U$ and $\frac{1}{2}\rho_l U^2$, and thus decreases as We increases ($h_{m,c} \propto Oh_{g,l}D/\sqrt{We}$). The fidelity of We' can be verified by the regime

Bouncing/coalescence transitions in binary droplet collisions

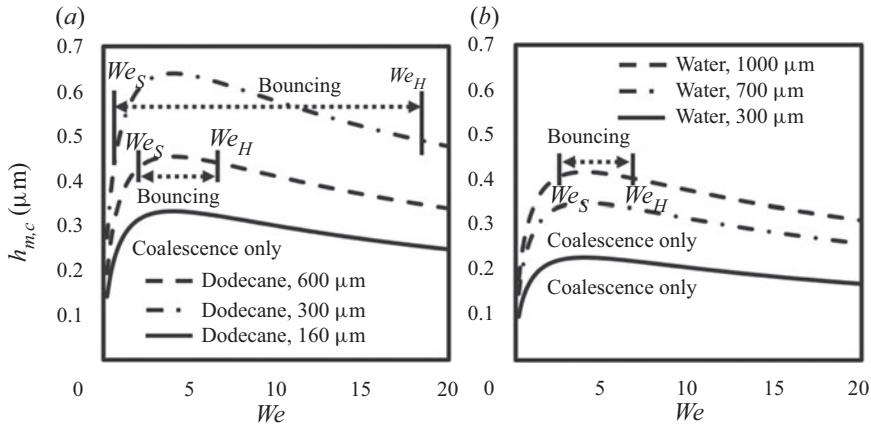


Figure 7. Characteristic minimum thickness of the gas film as a function of We in (3.9) for (a) dodecane and (b) water drops, where the experimentally obtained We_S and We_H are indicated.

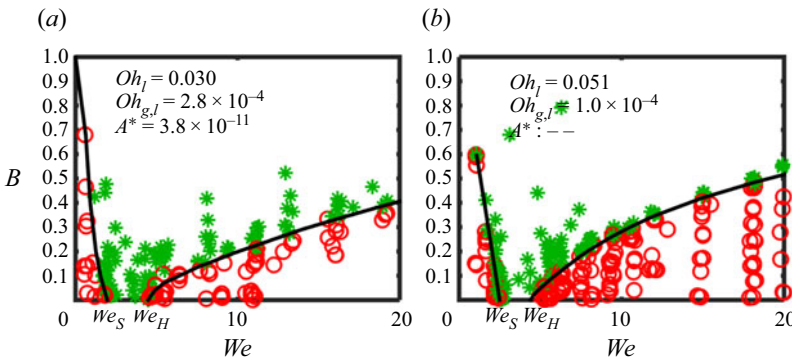


Figure 8. Regime diagram for (a) tetradecane drops with $D = 230 \mu\text{m}$ and $Oh_l = 0.030$ and (b) glycerol-water solution (60%) drops with $D = 450 \mu\text{m}$ and $Oh_l = 0.051$.

diagram shown in figures 1(a) and 8, and the available data for drop–drop collisions (Jiang *et al.* 1992), demonstrating the transitional We from PB to FB being located in the range 3.3 to 4.5 with $Oh_l = 0.006$ – 0.051 . Moreover, We' is almost the same as the mid-value of the bouncing range for droplets impacting a solid surface (de Ruiter *et al.* 2015). This justifies the same nature of droplet bouncing in drop–drop and drop–surface impacts for which the exclusive value of We' gives a universal outcome of the transition.

3.2.3. Effects of droplet size and fluid properties

Equation (3.9) describes the exclusive influence of droplet size found in the experiments. For the series of dodecane drops with $D = 300$ and $600 \mu\text{m}$, as shown in figure 7(a), We_S and We_H are located at the opposite sides of the corresponding maximum $h_{m,c}$ within which bouncing occurs and $h_{m,c}$ is larger than that outside where coalescence results. By decreasing D to $160 \mu\text{m}$, the $h_{m,c}$ values become the smallest compared with those for the other sizes of drops and no bouncing can be observed. The same evolution of We – $h_{m,c}$ curves with varying droplet size is also found for water drops as shown in figure 7(b). It is seen that at the smallest diameter ($300 \mu\text{m}$), the value of $h_{m,c}$ is the smallest compared

with that for the other droplet sizes. When D is increased to $1000\ \mu\text{m}$, the $h_{m,c}$ curve is raised and a bouncing regime is formed around the maximum value.

The effects of fluid properties such as surface tension on bouncing can also be realized via (3.9). Considering drops with identical D ($300\ \mu\text{m}$) but distinct surface tensions, bouncing occurs in cases of dodecane drops featuring a smaller surface tension and larger values of $h_{m,c}$ (figure 7a). On the other hand, water drops having a larger surface tension have rendered smaller values of $h_{m,c}$ (figure 7b), yielding only coalescence in head-on collisions. Surprisingly, comparing the cases showing similar magnitudes of $h_{m,c}$, i.e. dodecane drops with $D = 300\ \mu\text{m}$ (figure 7a) and water drops with $D = 1000\ \mu\text{m}$ (figure 7b), the values of We_S and We_H and hence the bouncing range are quite similar. This reveals the applicability of $h_{m,c}$ as an index for evaluation of bouncing in a head-on impact and hence the formation of a fully developed regime (II).

Figure 7 demonstrates a consistency between the trend predicted by (3.9) and the non-monotonic transitions of coalescence (I) to bouncing (II) and to coalescence (III) again in the regime diagrams depicted by the experimental results. This indicates that bouncing may occur when $h_{m,c}$ is sufficiently large, i.e. beyond a certain threshold, and can explain the influence of various fluid properties found in previous studies. For instance, the effect of droplet size mentioned by Li (2016) can be understood from figure 7, showing that a larger droplet diameter leads to a larger $h_{m,c}$ and thus promotes occurrence of bouncing. This scaling prediction unambiguously interprets the experimental finding of the present study of the development of the bouncing regime with varying droplet diameter and fluid properties. Specifically, (3.9) shows that $h_{m,c}$ increases as Oh_l or $Oh_{g,l}$ increases, which can be achieved by increasing μ_l or μ_g as discussed in previous work (Jiang *et al.* 1992; Qian & Law 1997; Estrade *et al.* 1999; Zhang & Law 2011; Tang *et al.* 2012; Kwakkel *et al.* 2013; Huang & Pan 2015; Li 2016; Pan *et al.* 2016; Sommerfeld & Kuschel 2016; Hu *et al.* 2017; Al-Dirawi & Bayly 2019), thus enhancing the propensity for droplet bouncing. On the contrary, a larger surface tension contributes to smaller Oh_l and $Oh_{g,l}$, leading to a smaller $h_{m,c}$ and thus to a higher tendency towards coalescence, as observed previously (Ashgriz & Poo 1990; Jiang *et al.* 1992; Qian & Law 1997; Estrade *et al.* 1999; Zhang & Law 2011).

3.3. Critical film thickness and criterion of droplet merging

The results in figure 7 indicate a consensus with previous understanding that droplet merging occurs if the minimum film thickness is small enough to be dominated by vdW forces (Gopinath & Koch 2002; Pan *et al.* 2008; Zhang & Law 2011; Li 2016; Chubynsky *et al.* 2020). To further assess the critical thickness, h_{cr} , in a quantitative manner, we consider the condition when the disjoining pressure given by the vdW force which tends to destabilize the interfaces becomes comparable to the capillary pressure of surface tension that is opposing the fluctuations (Vaynblat, Lister & Witelski 2001; Yoon *et al.* 2007; Ardekani & Joseph 2009; Thete *et al.* 2015). From the scaling relation, $A_H/6\pi h_{cr}^3 \sim 4\sigma/D$, we obtain h_{cr} and the dimensionless critical thickness:

$$H_{cr} = \frac{h_{cr}}{D} \sim \sqrt[3]{\frac{A_H}{24\pi\sigma D^2}} = \sqrt[3]{\frac{A^*}{24\pi}}, \quad (3.11)$$

where A_H is the Hamaker constant and $A^* = A_H/\sigma D^2$ the dimensionless Hamaker constant (Erneux & Davis 1993; Yoon *et al.* 2007; Ardekani & Joseph 2009). Critical thickness h_{cr} has long been studied (Ivanov *et al.* 1970; Ivanov 1988; Yoon *et al.* 2007; Ardekani & Joseph 2009; Kaur & Leal 2009) and found to depend mainly on the

dimensionless Hamaker constant (Yoon *et al.* 2007; Ardekani & Joseph 2009; Kaur & Leal 2009). Furthermore, in this scaling analysis, due to the neglecting of gas inertia in the lubrication equation as discussed, the effect of the Ohnesorge number of the gas film, i.e. $Oh_g = \mu_g / \sqrt{\rho_g D \sigma}$, is not considered. Therefore, the dominance of A^* on h_{cr}/D is justified as shown in (3.11). It is also noted that, while more complications could be rendered by varying B , here we consider only head-on collisions due to the significance in marking off the formation of a FB in binary droplet collisions.

In (3.11), the scaled values of h_{cr} , which is independent of We , are of the same order of magnitude as that approximated in previous studies (Yoon *et al.* 2007; Ardekani & Joseph 2009; Thete *et al.* 2015), showing that droplet merging occurs when the minimum thickness of the gas film falls in the range 100–1000 Å. This critical thickness suggests a threshold for determination of bouncing. Specifically, with reference to the non-monotonic trend shown by (3.9) in figure 7 and prior criterion of coalescence, if $h'_{m,c}$ is smaller than h_{cr} , the values of $h_{m,c}$ within the whole range of We are lower than that of h_{cr} , and thus coalescence dominates all the way in head-on collisions. Conversely, when $h'_{m,c}$ is larger than h_{cr} , bouncing can be created within some range of We in head-on collisions; thus a fully developed regime (II) is observable.

Based on these results, it is reasonable to propose a criterion specifying that, if $h'_{m,c}$ is larger than the critical film thickness, i.e. $h'_{m,c} > C_1 h_{cr}$, where C_1 is an empirical coefficient, bouncing can be generated in head-on impacts and thus the corresponding regime is fully developed in the diagram. With reference to the present and previous experimental data (Jiang *et al.* 1992; Tang *et al.* 2012; Sommerfeld & Kuschel 2016), the occurrence of a fully developed bouncing regime for different fluid properties is found to follow this criterion with the fitting coefficient $C_1 = 21.1$. Figure 9(a) shows that the regime diagrams with FB (open symbols) are all located above $h'_{m,c} = 21.1 h_{cr}$ (black solid line) and those exhibiting PB are below. Specifically, when surface tension decreases or the drop diameter increases, both $h'_{m,c}$ and h_{cr} increase, with the increase of h_{cr} being much less than that of $h'_{m,c}$. Consequently, when $h'_{m,c} > 21.1 h_{cr}$, i.e. $1.2 Oh_{g,l} / (1 - 2 Oh_l) > \sqrt[3]{A^*}$, the regime diagram transforms to that with FB, yielding bouncing in head-on collisions. In a more generic way, the present thickness-based criterion is manifested in a dimensionless form plotted in figure 9(b), where the effects of various fluid properties can be understood through the relation of $H'_{m,c}$ versus H_{cr} . By increasing $Oh_{g,l}$, e.g. by increasing gas viscosity or decreasing surface tension, a larger $H'_{m,c}$ results, thus encouraging droplet bouncing and FB. On the other hand, by decreasing D or increasing A_H , a larger H_{cr} is yielded, thus encouraging coalescence and PB. In addition, the influence of liquid viscosity on droplet bouncing is revealed by $H'_{m,c} = 6\mu_g / (1 - 2 Oh_l) \sqrt{\rho_l D \sigma}$, showing that increasing liquid viscosity increases $H'_{m,c}$ and hence enhances droplet bouncing. The parameters used in figure 9 can be seen in Appendix B.

The dimensionless parameters ($Oh_{g,l}$, Oh_l , A^*) used here are derived based on the physical principles that govern the hydrodynamics in colliding drops and intervening gas film, i.e. the momentum conservation in the liquid and gas phases and the stress balance on the liquid–gas interface (Pan *et al.* 2008; Zhang & Law 2011; Li 2016; Chubynsky *et al.* 2020), as well as the energy conservation in the liquid phase. By using these dimensionless parameters that can describe the bouncing/coalescent dynamics of two drops, the transition from PB to FB can be predicted not only for our experimental data, but also for other types of droplets such as alcohol, water and alkanes with different diameters (Jiang *et al.* 1992; Tang *et al.* 2012; Huang & Pan 2015; Sommerfeld & Kuschel 2016). The model proposed in the present study is applicable to all the existing data ($Oh_{g,l} = 0.7 \times 10^{-4} - 3.6 \times 10^{-4}$,

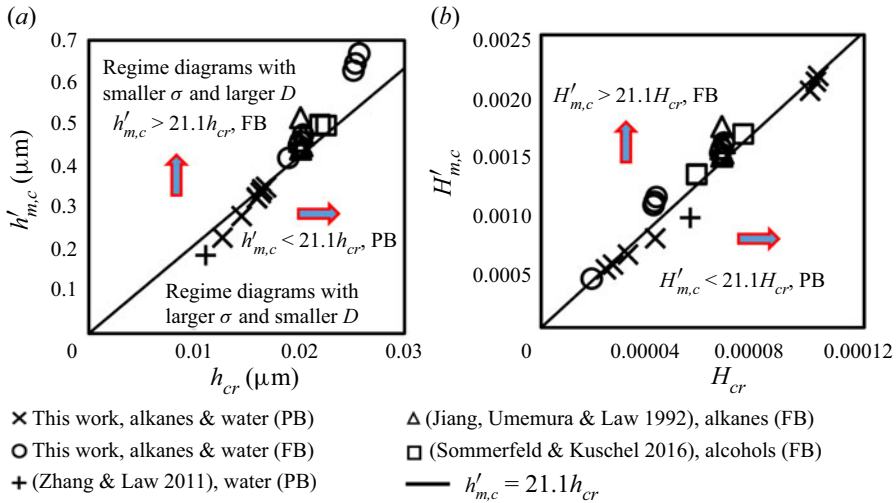


Figure 9. Graphs for predicting the occurrence of PB and FB at fixed dimensionless groups ($Oh_{g,l}$, Oh_l , A^*) with (a) dimensional thickness ($h'_{m,c}$, h_{cr}) and (b) dimensionless thickness ($H'_{m,c}$, H_{cr}). Here $H_{cr} = (A^*/24\pi)^{1/3}$ and $H'_{m,c} = 6Oh_{g,l}(1 - 2Oh_l)^{-1}$.

$Oh_l = 0.003\text{--}0.282$, $A^* = 5.1 \times 10^{-13}\text{--}8.21 \times 10^{-11}$), and it is reasonable to assume its validity for other droplet collision systems that are governed by the same physical laws.

4. Concluding remarks

We have experimentally demonstrated the unique effects of droplet size on bouncing phenomena in droplet collisions for alkanes, water and glycerol solutions having distinct properties. It is found that given a sufficiently large droplet diameter for water, the bouncing regime can extend from off-centre conditions to head-on impacts. Conversely, by decreasing the droplet size sufficiently, bouncing can be totally eliminated in head-on collisions of alkane drops. That is, bouncing is promoted by increasing droplet diameter but suppressed by decreasing it. By deriving the characteristic minimum thickness of the intervening gas film via a scaling analysis, we show that a larger $h_{m,c}$ yields a greater tendency to produce bouncing. The scaled $h_{m,c} \propto D$ is coincident with previous scaling results neglecting the effect of liquid viscosity, showing that the film thickness (h) increases as D increases (Mani, Mandre & Brenner 2010; Duchemin & Josserand 2011; Klaseboer *et al.* 2014). Moreover, by comparing the non-monotonic function of $h_{m,c}(We)$ and the threshold for droplet coalescence, h_{cr} , a scaling relation is established to determine whether bouncing can occur in head-on collisions. Therefore, the occurrence of the non-monotonic coalescence–bouncing–coalescence transitions can be foreseen by simply using the dimensionless group ($Oh_{g,l}$, Oh_l , A^*) without resorting to full-field numerical simulations that may account for more detailed structures such as rarefied gas dynamics and compressibility. The inevitably included sole coefficient is fitted from a large pool of available data covering the present and previous experimental results, which would apply to a considerable range of ($Oh_{g,l}$, Oh_l , A^*).

The effect of gas rarefaction has been indicated in previous models, showing that μ_g can be reduced by dividing a reduction factor, $\Delta(Kn)$, for h around the mean free path of gas (Pan *et al.* 2008; Li 2016; Chubynsky *et al.* 2020). Here $Kn = \lambda/h$, which is the Knudsen

Bouncing/coalescence transitions in binary droplet collisions

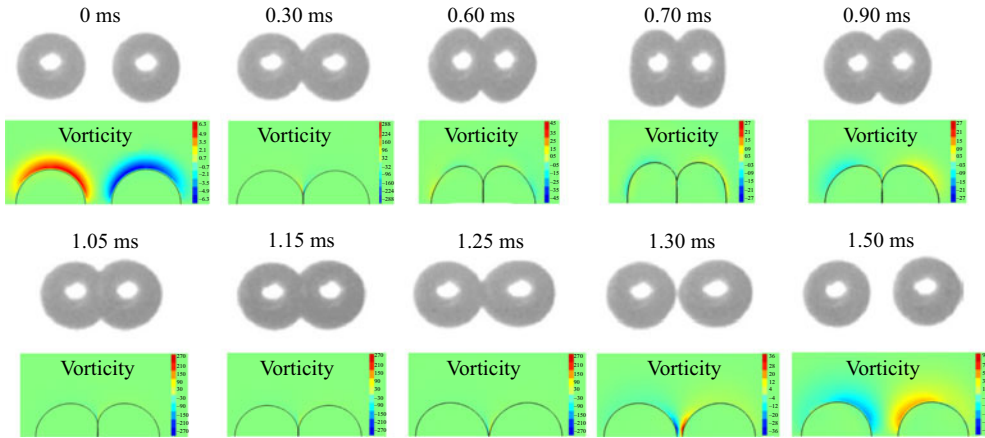


Figure 10. Comparison between the experimental images (Pan, Law & Zhou 2008) and the numerical simulation for bouncing tetradecane droplets of equal size ($D = 341.2 \mu\text{m}$ and $U = 0.486 \text{ m s}^{-1}$). The parameters used in the simulation are the same as the experimental conditions of Pan *et al.* (2008), where the colour bar indicates the magnitude of vorticity.

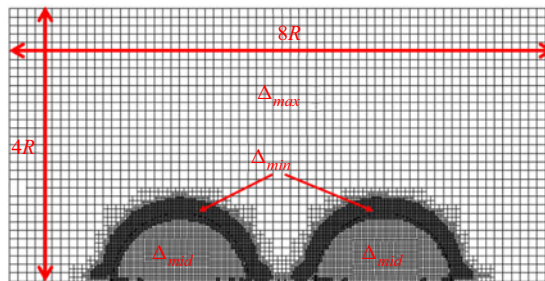


Figure 11. Schematic of initial computational domain.

number, and $\Delta(Kn) \geq 1$, increasing monotonically as Kn increases. Li (2016) stated that a larger D contributed to a smaller $\bar{\lambda}$, leading to a lesser reduction of μ_g and droplet bouncing. However, the reduction of μ_g is actually dominated by Kn (Pan *et al.* 2008; Li 2016; Chubynsky *et al.* 2020), indicating that a larger h contributes to a smaller Kn ($\propto 1/h$) and a lesser reduction of μ_g , thus promoting droplet bouncing. Surprisingly, based on the hydrodynamic scaling relations, the result of $h_{m,c} \propto D$ demonstrates the influence of drop size on bouncing, which is further modified by a congruent effect of rarefied gas dynamics, showing that $Kn \propto 1/h_{m,c}$. Consequently, the parametric influences on bouncing can be elucidated in terms of the macroscopic parameters.

Acknowledgement. We appreciate the experimental assistance of C.-J. Chang and C.-L. Hung.

Funding. We are grateful for the funding support of NTU Career Development Project (NTU-CDP-106R7822, NTU-107L7822, NTU-108L7822 and NTU-109L7822) and of MOST (109-2221-E-002-203 and 110-2221-E-002-088-MY3).

Declaration of interests. The authors report no conflict of interest.

Author ORCIDs.

 Kuo-Long Pan <http://orcid.org/0000-0001-6906-3323>.

Droplet diameter (μm)	Lens magnification	Spatial resolution (pixels mm^{-1})	Frame rate (frames per second)	Field of view (pixels ²)
160	4	200	42 000	256 × 240
300–600	2	100	10 000	512 × 512
700	1.5	75	10 000	512 × 512
1000	1	50	10 000	512 × 512

Table 3. Settings of high-speed camera.

	Refractive index n	Dielectric constant ϵ	Planck's constant h	Absorption frequency ν_e	Hamaker constant H_A
Decane	1.410	2.00	6.626×10^{-34}	3×10^{15}	5.0×10^{-20}
Dodecane	1.411	2.01	6.626×10^{-34}	3×10^{15}	5.0×10^{-20}
Tetradecane	1.428	2.04	6.626×10^{-34}	2.9×10^{15}	5.2×10^{-20}
Hexadecane	1.433	2.05	6.626×10^{-34}	2.9×10^{15}	5.3×10^{-20}
Water	1.333	78.5	6.626×10^{-34}	3×10^{15}	3.7×10^{-20}
Pentane	1.355	1.84	6.626×10^{-34}	3×10^{15}	3.9×10^{-20}
Hexanol	1.418	12.1	6.626×10^{-34}	3×10^{15}	5.5×10^{-20}
Heptanol	1.422	11.4	6.626×10^{-34}	3×10^{15}	5.8×10^{-20}
Dodecanol	1.44	6.4	6.626×10^{-34}	3×10^{15}	5.6×10^{-20}

Table 4. Properties of tested liquids (25 °C).

Appendix A. Experimental methodology

The field of view and frame rate for every collision event depend on the droplet diameter and [table 3](#) indicates the corresponding settings.

Appendix B. Calculation of Hamaker constant

To estimate the critical thickness (h_{cr}) between two drops, the Hamaker constants of various liquids are evaluated and listed in [table 4](#). The quantities are calculated by the Lifshitz theory considering two identical masses of liquids in proximity in vacuum/air (Lifshitz 1956; Israelachvili 2011), showing that

$$A_H = \frac{3}{4}KT \left(\frac{\epsilon - 1}{\epsilon + 1} \right)^2 + \frac{3h\nu_e}{16\sqrt{2}} \frac{(n^2 - 1)^2}{(n^2 + 1)^{3/2}}. \quad (\text{B1})$$

Appendix C. Derivation of the momentum equation for the droplet

The momentum equation (3.2) is derived from the projection of the quasi-steady Navier–Stokes equation along the streamline (Spivak *et al.* 2002), showing that

$$\frac{1}{\rho} \frac{\partial P}{\partial s} + V_s \frac{\partial V_s}{\partial s} + V_n \frac{\partial V_n}{\partial n} = V \times \omega - \nu(\nabla \times \omega) = V_z \omega_n - V_n \omega_z - \nu \left(\frac{\partial \omega_z}{\partial n} - \frac{\partial \omega_n}{\partial z} \right). \quad (\text{C1})$$

Here the subscript s denotes the direction along the streamline and n denotes the direction normal to the streamline. In the present scenario, $\omega_n = V_n = V_z = 0$, and thus (C1)

Gas viscosity μ_g (mPa s)	Liquid viscosity μ_l (mPa s)	Gas density ρ_g (kg m ⁻³)	Liquid density ρ_l (kg m ⁻³)	Surface tension σ (mN m ⁻¹)	Radius R (μm)
0.00168	2.05	1.2	744	24.9	170.6

Table 5. Properties of tetradecane drops (25 °C).

becomes

$$\frac{1}{\rho} \frac{\partial P}{\partial s} + V_S \frac{\partial V_S}{\partial s} = \nu \frac{\partial \omega_z}{\partial n}, \quad (\text{C2})$$

or in dimensionless form

$$\frac{\partial \bar{P}}{\partial \bar{s}} + \bar{V}_S \frac{\partial \bar{V}_S}{\partial \bar{s}} = \frac{1}{Re_l} \frac{\partial \bar{\omega}_z}{\partial \bar{n}}. \quad (\text{C3})$$

Here $Re_l = \rho_l UD / \mu_l$, which is the Reynolds number of the droplet. Based on the numerical simulation (figure 10), the magnitude of vorticity in the droplet is very small, which is at least 20 times smaller than that in the gas phase. In addition, since $1/Re_l < 0.05$ in the present study, we neglect $\nu(\partial \omega_z / \partial n)$ and (C2) becomes

$$\frac{1}{\rho} \frac{\partial P}{\partial s} + V_S \frac{\partial V_S}{\partial s} = \nabla_s \left(\frac{P}{\rho} + \frac{1}{2} V_S^2 \right) = 0. \quad (\text{C4})$$

This result shows that the momentum equation with the viscous term has the same form as the Bernoulli equation when it is projected along the streamline. Thus we assume that the droplet is viscous while the Bernoulli equation is valid for describing the momentum distribution in the droplet.

Appendix D. Numerical setting of the simulation in Appendix C

To understand the vorticity distribution in the droplets during the bouncing process, here we reproduce a previous experimental case (Pan *et al.* 2008) using GERRIS open source code (Popinet 2003, 2009). The initial computational domain of GERRIS axisymmetric simulation is shown in figure 11, where the centres of two identical droplets are placed on the symmetry axis with a separation distance of $3R$, each given a velocity magnitude of $U/2$ but in opposite directions. The computational boundaries are set to have zero gradients for velocities, i.e. Neumann conditions, and fixed pressure at zero, i.e. Dirichlet conditions. The adaptive mesh refinement, with three different initial mesh sizes $(\Delta_{max}, \Delta_{mid}, \Delta_{min}) = (R/2^3, R/2^5, R/2^6)$, is performed in the computations to facilitate numerical simulations, where Δ_{max} is set in the gas phase, Δ_{min} in the liquid–gas interface and Δ_{mid} in the liquid phase and high-vorticity region of the gas phase. To resolve the dynamics of the gas film, Δ_{min} is set to $R/2^{10}$ (166 nm). By using a Courant–Friedrichs–Lewy (CFL) number of 0.2 and the physical parameters as listed in table 5, the experimental results can be reproduced by the simulations with the same impact conditions, as shown in figure 10.

REFERENCES

- AL-DIRAWI, K.H. & BAYLY, A.E. 2019 A new model for the bouncing regime boundary in binary droplet collisions. *Phys. Fluids* **31** (2), 027105.

- ARDEKANI, A.M. & JOSEPH, D.D. 2009 Instability of stationary liquid sheets. *Proc. Natl Acad. Sci. USA* **106** (13), 4992–4996.
- ASHGRIZ, N. & POO, J.Y. 1990 Coalescence and separation in binary collisions of liquid drops. *J. Fluid Mech.* **221**, 183–204.
- BRENN, G., VALKOYSKA, D. & DANOV, K.D. 2001 The formation of satellite droplets by unstable binary drop collisions. *Phys. Fluids* **13** (9), 2463–2477.
- CHIU, H.H. 2000 Advances and challenges in droplet and spray combustion. I: toward a unified theory of droplet aerothermochemistry. *Prog. Energy Combust. Sci.* **26**, 381–416.
- CHUBYNSKY, M.V., BELOUSOV, K.I., LOCKERBY, D.A. & SPRITTLES, J.E. 2020 Bouncing off the Walls: The Influence of Gas-Kinetic and van der Waals Effects in Drop Impact. *Phys. Rev. Lett.* **124** (8), 084501.
- DUCHEMIN, L. & JOSSEERAND, C. 2011 Curvature singularity and film-skating during drop impact. *Phys. Fluids* **23** (9), 091701.
- ERNEUX, T. & DAVIS, S.H. 1993 Nonlinear rupture of free films. *Phys. Fluids A* **5** (5), 1117–1122.
- ESTRADE, J.P., CARENTZ, H., LAVERGNE, G. & BISCOS, Y. 1999 Experimental investigation of dynamic binary collision of ethanol droplets—a model for droplet coalescence and bouncing. *Intl J. Heat Fluid Flow* **20** (5), 486–491.
- FENG, Y., KLEINSTREUER, C., CASTRO, N. & ROSTAMI, A. 2016 Computational transport, phase change and deposition analysis of inhaled multicomponent droplet–vapor mixtures in an idealized human upper lung model. *J. Aerosol Sci.* **96**, 96–123.
- FINOTELLO, G., KOOIMAN, R.F., PADDING, J.T., BUIST, K.A., JONGSMA, A., INNINGS, F. & KUIPERS, J.A.M. 2018 The dynamics of milk droplet–droplet collisions. *Exp. Fluids* **59** (1), 17.
- GOPINATH, A., CHEN, S.B. & KOCH, D.L. 1997 Lubrication flows between spherical particles colliding in a compressible non-continuum gas. *J. Fluid Mech.* **344**, 245–269.
- GOPINATH, A. & KOCH, D.L. 2002 Collision and rebound of small droplets in an incompressible continuum gas. *J. Fluid Mech.* **454**, 145–201.
- GRALTON, J., TOVEY, E., MCLAWS, M.L. & RAWLINSON, W.D. 2011 The role of particle size in aerosolised pathogen transmission: a review. *J. Infect.* **62** (1), 1–13.
- GUNN, R. 1965 Collision characteristics of freely falling water drops. *Science* **150**, 695–701.
- HU, C., XIA, S., LI, C. & WU, G. 2017 Three-dimensional numerical investigation and modeling of binary alumina droplet collisions. *Intl J. Heat Mass Transfer* **113**, 569–588.
- HUANG, K.L. & PAN, K.L. 2015 Size effect on the transition from coalescence to bouncing regime in binary droplet. In *13th Triennial International Conference on Liquid Atomization and Spray Systems, Tainan, Taiwan, August 23–27*.
- HUANG, K.L., PAN, K.L. & JOSSEERAND, C. 2019 Pinching Dynamics and Satellite Droplet Formation in Symmetrical Droplet Collisions. *Phys. Rev. Lett.* **123** (23), 234502.
- ISRAELACHVILI, J.N. 2011 *Intermolecular and Surface Forces*, 3rd edn. Academic.
- IVANOV, I.B., RADOEV, B., MANEV, E. & SCHELUDKO, A. 1970 Theory of the critical thickness of rupture of thin liquid films. *Transactions of the Faraday Society* **66**, 1262–1273.
- IVANOV, I.B. 1988 *Thin Liquid Films*. Marcel Dekker.
- JIANG, Y.J., UMEMURA, A. & LAW, C.K. 1992 An experimental investigation on the collision behaviour of hydrocarbon droplets. *J. Fluid Mech.* **234**, 171–190.
- KAUR, S. & LEAL, L.G. 2009 Three-dimensional stability of a thin film between two approaching drops. *Phys. Fluids* **21** (7), 072101.
- KLASEBOER, E., MANICA, R. & CHAN, D.Y.C. 2014 Universal behavior of the initial stage of drop impact. *Phys. Rev. Lett.* **113**, 194501.
- KWAKKEL, M., BREUGEM, W.-P. & BOERSMA, B.J. 2013 Extension of a CLSVOF method for droplet-laden flows with a coalescence/breakup model. *J. Comput. Phys.* **253**, 166–188.
- LI, J. 2016 Macroscopic model for head-on binary droplet collisions in a gaseous medium. *Phys. Rev. Lett.* **117** (21), 214502.
- LIFSHITZ, E. 1956 The Theory of Molecular Attractive Forces between Solids. *Soviet Phys.* **2** (1), 73.
- MANI, M., MANDRE, S. & BRENNER, M.P. 2010 Events before droplet splashing on a solid surface. *J. Fluid Mech.* **647**, 163–185.
- MANICA, R. & CHAN, D.Y. 2011 Drainage of the air–water–quartz film: experiments and theory. *Phys. Chem. Chem. Phys.* **13** (4), 1434–1439.
- MANICA, R., PARKINSON, L., RALSTON, J. & CHAN, D.Y. 2010 Interpreting the dynamic interaction between a very small rising bubble and a hydrophilic titania surface. *J. Phys. Chem. C* **114** (4), 1942–1946.
- MAY, K.R. 1973 The Collision nebulizer: description, performance and application. *J. Aerosol Sci.* **4** (3), 235–243.
- PAN, K.L. 2004 Dynamics of droplet collision and flame-front motion. PhD thesis, Princeton University.

Bouncing/coalescence transitions in binary droplet collisions

- PAN, K.L., CHOU, P.C. & TSENG, Y.J. 2009 Binary droplet collision at high Weber number. *Phys. Rev. E* **80**, 036301.
- PAN, K.L., HUANG, K.L., HSIEH, W.T. & LU, C.R. 2019 Rotational separation after temporary coalescence in binary droplet collisions. *Phys. Rev. Fluids* **4** (12), 123602.
- PAN, K.L. & LAW, C.K. 2004 On the dynamics of head-on droplet collision: experiment and simulation. *AIAA Paper* 2004-1159.
- PAN, K.L., LAW, C.K. & ZHOU, B. 2008 Experimental and mechanistic description of merging and bouncing in head-on binary droplet collision. *J. Appl. Phys.* **103**, 064901.
- PAN, K.L., TSENG, Y.H., CHEN, J.C., HUANG, K.L., WANG, C.H. & LAI, M.C. 2016 Controlling droplet bouncing and coalescence with surfactant. *J. Fluid Mech.* **799**, 603–636.
- PARKINSON, L. & RALSTON, J. 2010 The interaction between a very small rising bubble and a hydrophilic titania surface. *J. Phys. Chem. C* **114** (5), 2273–2281.
- POPINET, S. 2003 Gerris: a tree-based adaptive solver for the incompressible Euler equations in complex geometries. *J. Comput. Phys.* **190**, 572–600.
- POPINET, S. 2009 An accurate adaptive solver for surface-tension-driven interfacial flows. *J. Comput. Phys.* **228**, 5838–5866.
- QIAN, J. & LAW, C.K. 1997 Regimes of coalescence and separation in droplet collision. *J. Fluid Mech.* **331**, 59–80.
- REITTER, L., LIU, M., BREITENBACH, J., HUANG, K.L., BOTHE, D., BRENN, G., PAN, K.L., ROISMAN, I.V., & TROPEA, C. 2017 Experimental and computational investigation of binary drop collisions under elevated pressure. In *Illass Europe. 28th European Conference on Liquid Atomization and Spray Systems, Spain, València, September 6–8*.
- DE RUITER, J., LAGRAAUW, R., VAN DEN ENDE, D. & MUGELE, F. 2015 Wettability-independent bouncing on flat surfaces mediated by thin air films. *Nat. Phys.* **11**, 48–53.
- SOMMERFELD, M. & KUSCHEL, M. 2016 Modelling droplet collision outcomes for different substances and viscosities. *Exp. Fluids* **57** (12), 187.
- SPIVAK, B., VANDEN-BROECK, J.M. & MILOH, T. 2002 Free-surface wave damping due to viscosity and surfactants. *Eur. J. Mech. B/Fluids* **21** (2), 207–224.
- STRANGWAYS, I. 2006 *Precipitation: Theory, Measurement and Distribution*. Cambridge University Press.
- TANG, C., ZHANG, P. & LAW, C.K. 2012 Bouncing, coalescence, and separation in head-on collision of unequal-size droplets. *Phys. Fluids* **24**, 022101.
- TELLIER, R. 2009 Aerosol transmission of influenza A virus: a review of new studies. *J. R. Soc. Interface* **6**, S783–S790.
- THETE, S.S., ANTHONY, C., BASARAN, O.A. & DOSHI, P. 2015 Self-similar rupture of thin free films of power-law fluids. *Phys. Rev. E* **92** (2), 023014.
- VAYNBLAT, D., LISTER, J.R. & WITELSKI, T.P. 2001 Rupture of thin viscous films by van der Waals forces: Evolution and self-similarity. *Phys. Fluids* **13**, 1130–1140.
- YIANTSIOS, S.G. & DAVIS, R.H. 1990 On the buoyancy-driven motion of a drop towards a rigid surface or a deformable interface. *J. Fluid Mech.* **217**, 547–573.
- YOON, Y., BALDESSARI, F., CENICEROS, H.D. & LEAL, L.G. 2007 Coalescence of two equal-sized deformable drops in an axisymmetric flow. *Phys. Fluids* **19** (10), 102102.
- ZHANG, D., ZHANG, P., YUAN, Y. & ZHANG, T. 2016 Hypergolic ignition by head-on collision of *N,N,N',N'*-tetramethylethylenediamine and white fuming nitric acid droplets. *Combust. Flame* **173**, 276–287.
- ZHANG, P. & LAW, C.K. 2011 An analysis of head-on droplet collision with large deformation in gaseous medium. *Phys. Fluids* **23**, 042102.